

Special
Collection

Realigning the Chemistry and Parameterization of Lithium-Sulfur Battery Models to Accommodate Emerging Experimental Evidence and Cell Configurations

Caitlin D. Parke,^[a] Akshay Subramaniam,^[a] Venkat R. Subramanian,^[b] and Daniel T. Schwartz^{*[a]}

Experimental insights into lithium-sulfur (LiS) battery chemistry have resulted in practical improvements in cell coulombic efficiency, sulfur utilization, and cycle life. However, optimization of this complex battery chemistry requires experimentally aligned modeling tools. A porous electrode theory-based model incorporating key electrolyte dissociation chemistry is developed for the LiS cell. The proposed chemistry produces a radical anion species that is widely observed spectroscopically in LiS

electrolytes. We explore the implications of radical anion formation on the current-voltage behavior within the context of a state-of-art high energy density LiS cell with low electrolyte:sulfur (E/S) ratio and ideally-protected anode. Parameters describing the dissociation reaction equilibrium and kinetics are shown to alter the electrolyte speciation in ways that can be linked to observations from LiS electrolyte engineering experiments.

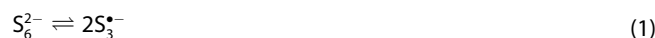
Introduction

As lithium ion batteries reach their theoretical limits, lithium sulfur (LiS) chemistry is emerging as a promising next-generation battery with high energy density to meet the burgeoning demands for electric transport applications. Lithium sulfur batteries have a theoretical energy density of 2600 Wh/kg, and some companies are claiming 400 Wh/kg already.^[1] The challenges facing adoption of this chemistry include poor cycle life, low Coulombic efficiency, and loss of active material during cycling.^[2]

For practical lithium sulfur batteries, polysulfide speciation and transport in the electrolyte, so-called polysulfide shuttling, is central to understanding LiS performance. Specifically, soluble higher-order polysulfide anions form during discharge and their transport to the anode leads to deleterious reactions with the lithium metal.^[3,4] Protection of reactive lithium surfaces, either through formation of a stable solid-electrolyte interface (SEI) or via engineered coatings, is crucial to cyclability.^[5] The sulfur in a fully charged cathode is insulating, as is the conversion product $\text{Li}_2\text{S}_{(s)}$ in a fully discharged cathode. Thus, the conductivity of the cathode is typically enhanced by making a porous sulfur/

carbon composite electrode, lowering the energy density of the cell.^[6] During discharge, the distribution of precipitated $\text{Li}_2\text{S}_{(s)}$ within the composite cathode can contribute to passivation and poor sulfur utilization.^[7] Ultimately, the electrolyte formulation plays an especially important role in this battery chemistry and makes up a large amount of the overall weight (about 40% in a calculation for 300 Wh/kg cell).^[8] To support the highest practical energy densities, the experimental trend is toward “lean” cells with ever lower electrolyte to sulfur ratios (E/S).^[1,9,10]

Electrolyte engineering—the design of solvent, salt, and additive systems—has profound impact on the shape of the voltage curve, cell capacity, and cyclability, owing to changes in soluble polysulfide speciation, insoluble product formation, conductivity, and reactivity with the anode.^[5,11–14] Experimental methods such as *in situ* Raman spectroscopy have proven valuable for showing how specific additives^[15] and ether-based electrolytes^[16] can alter speciation between long and short-chain polysulfides within the electrolyte, while also squelching or promoting stable formation of polysulfide radicals such as $\text{S}_3^{\bullet-}$. Likewise, the effects of varying solvent donor numbers (DN) on polysulfide speciation has been probed using UV-Vis spectroscopy,^[17] a technique that is sensitive to a wide array of polysulfide species.^[18,19] It was shown that solvent choice significantly impacts homogeneous chemistry in the electrolyte, sometimes favoring the stable formation of radical anion $\text{S}_3^{\bullet-}$ from its dimer anion S_6^{2-} via the dissociation reaction [Eq. (1)]^[17]



Though quantitative experimental measures of all the polysulfide species concentrations under battery-like operating conditions have not been reported, *in situ* and *operando* spectroscopy experiments clearly show the balance of species in dissociation Equation (1) are strongly modulated by electro-

[a] C. D. Parke, A. Subramaniam, Prof. D. T. Schwartz
Department of Chemical Engineering
University of Washington
Seattle, WA 98195, USA
E-mail: dts@uw.edu

[b] Prof. V. R. Subramanian
Walker Department of Mechanical Engineering &
Material Science Engineering
Texas Materials Institute, The University of Texas at Austin
Austin, TX 78712, USA

 Supporting information for this article is available on the WWW under <https://doi.org/10.1002/celec.202001575>

 An invited contribution to a joint Special Collection between ChemElectroChem and Batteries & Supercaps dedicated to research Beyond Lithium-Ion Batteries

lyte engineering strategies, along with the overall discharge behavior of LiS batteries.

Physics-based modeling of batteries seeks to integrate experimentally-relevant chemistry and transport in ways that yield important insights about system performance and key underlying mechanisms. Modeling studies for lithium sulfur batteries began in 2004 with a lumped model that described thermodynamics and kinetics primarily with a simplified reaction scheme.^[3] In 2008, Kumaresan et al.^[20] developed what has become the *de facto* standard one-dimensional model (1D) for LiS batteries. Kumaresan et al. included a multi-step sulfur reduction cascade with several soluble polysulfide intermediates and the insoluble $\text{Li}_2\text{S}_{(s)}$ precipitate, morphology evolution, kinetics, transport, and thermodynamics to describe lithium sulfur battery behavior. Since 2008, there have been quite a few studies to reconcile differences between experimental observations and the original Kumaresan et al. model, but there has been no fundamental reconsideration of polysulfide chemistry and speciation within full-cell continuum modeling, despite advances in understanding of electrolyte homogeneous chemistry driven by *in situ* and *operando* spectroscopy experiments.

For example, Ghaznavi et al. probed the parameter space of Kumaresan's model, and found that the model was only suitable for representing the discharge curve, and failed upon charging.^[21–23] Neidhardt et al. published a similar model^[24] and later explored impedance^[25] and capacity fade through polysulfide shuttle.^[26] Further work assumed trapped polysulfides and modeled only lithium ion transport within a nanostructured cathode.^[27] A study by Zhang et al. with a lumped model added electrolyte conductivity to better match experimental impedance data.^[28] Moy et al. developed a one-dimensional model for shuttle current under constant voltage operation; their work was combined with experimental efforts involving the additive LiNO_3 that is purported to suppress the polysulfide shuttling.^[29] With a simplified two-step reduction scheme, Marinescu and associates published a lumped model that described charge and discharge with precipitation of lithium sulfide.^[30] Zhang et al. concluded that the ionic diffusion coefficients within the Kumaresan model needed to be decreased by a factor of 100 to introduce rate dependencies seen in experimental work.^[31] A study by Yoo et al. modified the precipitation terms of the Kumaresan model to alleviate numerical instabilities and show reasonable charging curves,^[32] but the results have proven difficult to reproduce.^[33]

Similarly, work by Ren et al. focused on improving the precipitation kinetics through rate-dependent precipitation with experimental validation through SEM characterization of electrodes.^[34] A discharge model based on concentrated solution theory was developed by Mistry and Mukherjee that focused on the transport dynamics.^[35] Marinescu et al. studied degradation and classified capacity loss as reversible from chemical dissolution issues or irreversible from the polysulfide shuttling.^[36] Shim et al.^[37] published a study that combined experimental work and model work to explore the effect of LiNO_3 that may promote formation of an irreversible solid product within the cathode. With excessive additive, their

results showed distortion of the voltage curve with a third plateau at the end of discharge, and the modeling was able to replicate this feature by decreasing the rate of the last reduction reaction, which caused a third voltage drop and distinct precipitation regimes of $\text{Li}_2\text{S}_{2(s)}$ and $\text{Li}_2\text{S}_{(s)}$. Work by Kamyab et al. reported updated $\text{Li}_2\text{S}_{(s)}$ precipitation parameters that work for charging and studied the effect of polysulfide shuttle on cycling.^[33]

Our recently published work detailed a reduced-order model with decreased computational footprint that lacked spatially-resolved speciation, but still incorporates transport effects between electrode and separator compartment.^[38] Here we rely on macrohomogeneous porous electrode theory to represent the 1-D spatial variation of all species across the complex sulfur/carbon composite cathode and separator, as shown in Figure 1. More sophisticated models for cathode structure have explicitly incorporated the influence of multi-scale hierarchy in the sulfur-infused mesoporous carbon particles.^[39] While our focus here is on aligning the modeled electrolyte chemistry to observed electrolyte speciation, future work may benefit from more multiscale models of the cathode itself.

Although battery modeling has not yet incorporated electrolyte chemistry such as Equation (1) to understand its potential impact on whole-cell performance, sophisticated electroanalytical models by Thangavel et al.^[40] have. In particular, Thangavel et al. performed cyclic voltammetry (CV) experiments in a three electrode cell using a planar glassy carbon working electrode in an electrolyte with Li_2S_8 or Li_2S_6 as the (initial) electroactive species in 1 M LiTFSI supported TEGDME: DOL electrolyte. A 1D model of the working electrode and adjacent electrolyte diffusion layer could not describe experimental CV results using the original reduction chemistry cascade proposed by Kumaresan et al. With the addition of an alternative reaction pathway involving $\text{S}_3^{* -}$ and $\text{S}_2^{* -}$ species, the entire CV was successfully modeled and a set of reaction parameters were estimated. The work by Thangavel et al. represents one of the most promising ways to explore coupled electrochemical/chemical polysulfide chemistry and extract meaningful parameters that can be adapted to the more complex battery configuration where the anode and cathode are strongly coupled because of the small electrolyte volumes and high surface area electrodes.

Other issues associated with aligning current modeling with trends in experimental research, beyond electrolyte speciation, are small but worth acknowledging. For example, the extensive experimental literature that documents how to build high energy density cells includes critical parameter ranges for sulfur areal loading and weight percent, E/S ratios, cathode thicknesses, and porosities; these parameters are often easily related to the volume fractions, porosities, and thicknesses preferred by modelers. Less straightforward is relating the E/S ratio between experiments and modeling. Generally, E/S ratio is taken as an independent parameter in experiments that can be varied for a given electrode and separator sandwich. In contrast, the E/S ratio in a 1D model is set by cathode/separator/anode sandwich geometry, combined with the assumption of a fully-wetted

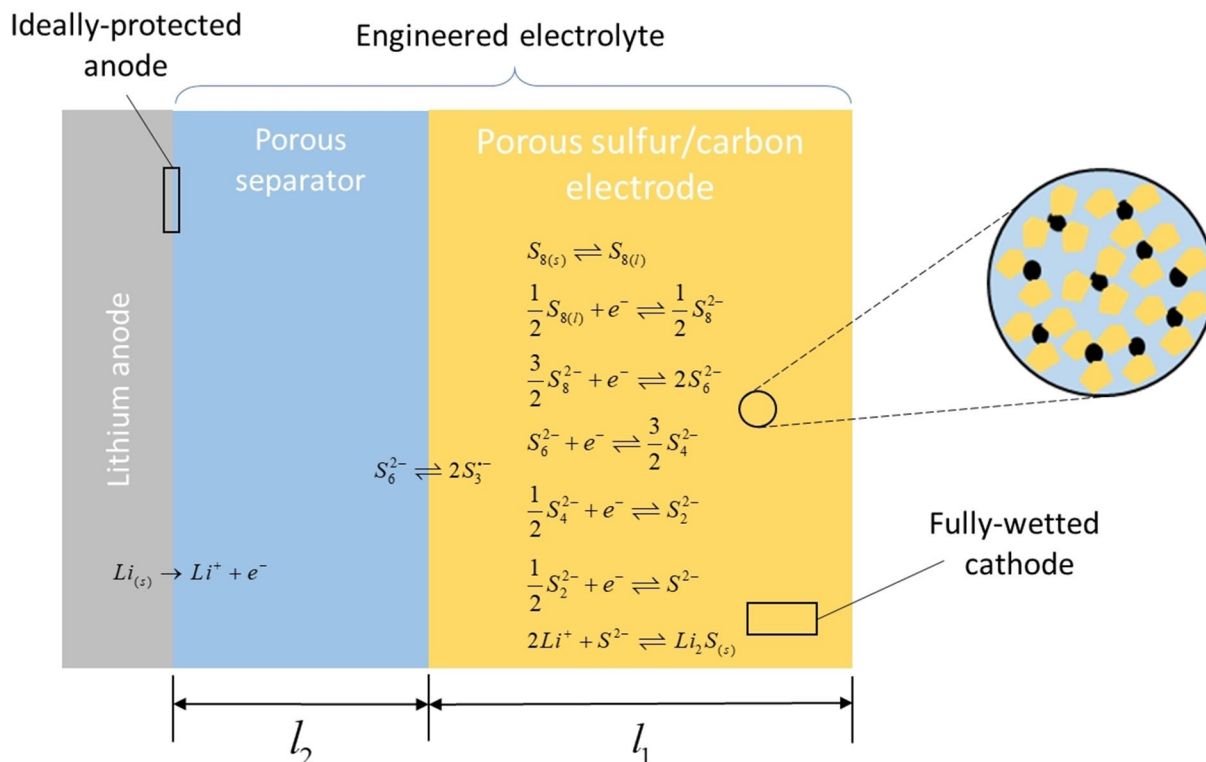


Figure 1. Schematic of lithium-sulfur sandwich layer with lithium anode, porous separator, and composite cathode with yellow solid sulfur particles, black conductive carbon, and binder.

pore-volume. The only way to change the E/S ratio in a 1D model is to change the pore volume of the separator and electrodes. For this model, the E/S ratio is fixed by cell geometry to a value just below 2 mL/g, which is at the highest energy-density end of experimentally-relevant values.

The work herein fundamentally builds off the Kumaresan et al. model of a LiS cell, as shown schematically in Figure 1. Updated geometric parameters in Table 1 correspond to high energy density lithium sulfur batteries, calculated according to estimates for a 300 Wh/kg pouch cell.^[8] Our base case uses the most experimentally-relevant physicochemical parameters available in the battery modeling literature. Inclusion of the electrolyte chemistry shown in Equation (1) allows for the generation

of S_3^{*-} radical, an electrolyte species widely observed in lithium sulfur battery studies.^[41–46] By adding Equation (1), we can explore, for the first time, how this homogenous, non-charge-transfer dissociation reaction is linked to the discharge behavior of a lithium sulfur battery with state-of-art geometric and physicochemical parameters.

Results and Discussion

To modernize the lithium sulfur electrochemical model and update it to match current understanding of the complex interdependence of electrolyte, additives, and speciation, new chemistry has been included. Specifically, dissociation of polysulfide anions into constituent radical anions has been reported in many experimental papers.^[16–17,41–42,45,48–50] We take this dissociation reaction to be a reversible, non-charge transfer reaction occurring homogeneously in the electrolyte according to Equation (1). Because the reaction is presumed reversible and elementary as written, the forward and backward reaction rates are $R_f = k_f [S_6^{2-}]$ and $R_b = k_b [S_3^{*-}]^2$. At equilibrium, the reaction rates will be equal, which allows us to define a reaction equilibrium constant, K_{S_3} [Eq. (2)]

$$K_{S_3} = \frac{k_f}{k_b} = \frac{[S_3^{*-}]^2}{[S_6^{2-}]} \quad (2)$$

Table 1. Geometric parameters for 300 Wh/kg.	
Parameter	Value
Sulfur content in cathode [wt %]	60 %
Areal sulfur loading [mg/cm ²]	4.9
Sulfur volume fraction ^[a]	0.24
Cathode thickness [μm] ^[a]	100
Separator Thickness [μm] ^[a]	20
E/S ratio [mL/g]	1.45
Cathode porosity ^[a]	0.60
Separator porosity ^[a]	0.60
Carbon/binder volume fraction ^[a]	0.16
Areal capacity [mAh/cm ²]	4.9
Cathode specific capacity [mAh/g]	1005

[a] Input parameters to the model.

where the square brackets denote the activity of the respective polysulfide species, which is assumed to be the concentration here. This reversible reaction is a sink for S_6^{2-} ions and the only source of the S_3^{*} -radical species. In particular, the newly modified species balance for S_6^{2-} is [Eq. (3)]

$$\frac{\partial \varepsilon C_{S_6^{2-}}}{\partial t} = -\frac{\partial N_{S_6^{2-}}}{\partial x} + r_{S_6^{2-}} - \varepsilon k_f \left(C_{S_6^{2-}} - \frac{C_{S_3^{*}}^2}{K_{S_3}} \right) \quad (3)$$

where ε is the porosity, $C_{S_6^{2-}}$ is the concentration of S_6^{2-} , $N_{S_6^{2-}}$ is the flux that includes diffusion and migration of S_6^{2-} , $r_{S_6^{2-}}$ is the rate of the electrochemical reactions that include S_6^{2-} , $C_{S_3^{*}}$ is the concentration of S_3^{*} species. The S_6^{2-} anion is directly involved in the electrochemical reduction cascade on the cathode. A wholly new species balance is added to the Kumaresan et al. model for the radical anion S_3^{*} species [Eq. (4)]

$$\frac{\partial \varepsilon C_{S_3^{*}}}{\partial t} = -\frac{\partial N_{S_3^{*}}}{\partial x} + 2\varepsilon k_f \left(C_{S_6^{2-}} - \frac{C_{S_3^{*}}^2}{K_{S_3}} \right) \quad (4)$$

We assume the S_3^{*} species does not directly participate in the electrochemical reduction cascade on the cathode, and can only influence the discharge curve by acting as a sink for S_6^{2-} species, which then is not available to react within the reduction cascade. The dissociation reaction parameters k_f and K_{S_3} , respectively dictate the time-scale for Equation (1) and the equilibrium distribution of the two species involved in Equation (1). The complete set of equations for the lithium sulfur electrochemical model is included as Table 2.

In addition to updating the reaction speciation, the physicochemical parameters have been updated to reflect the latest experimental and modeling literature on high energy density LiS batteries. For example, our group published updated thermodynamic parameters (Table 3) so that the high voltages observed in experimental discharge data from a pre-commercial high-energy density LiS pouch cell were adequately reflected in our modeled discharge curves.^[38] Therefore, our base case thermodynamic parameters presented here now reproduce voltages seen in state-of-art cells.

Other parameters used in our base-case simulations have also been qualitatively ground-truthed against experimental observations. For example, the diffusion coefficients from the Kumaresan et al. model do not adequately reproduce the C-rate dependencies seen in sulfur utilization and capacity experiments and need to be reduced by 1–2 orders of magnitude to observe expected transport limitations at higher rates.^[31] Our base case transport parameters in Table 4 reflect those findings, and also include a diffusion coefficient for the new radical anion species comparable to other shorter-chain polysulfide species. The remaining parameters are reported in Table 5 and Table 6, and represent values consistent with a high energy density LiS cell.

Figure 2 shows pairs of simulated voltage response curves for a high energy density cell using the new experimentally-aligned base case parameters developed here compared to the

Table 2. 1-D Lithium Sulfur Mathematical Discharge Model.^[a]

Governing equations	Boundary conditions
Positive electrode (Region 1) $\frac{\partial \varepsilon_1 C_{Li}}{\partial t} = -\frac{\partial N_{Li}}{\partial x} + r_i - R_i$ $\frac{\partial \varepsilon_1 C_{1,S_6^{2-}}}{\partial t} = -\frac{\partial N_{1,S_6^{2-}}}{\partial x} + r_{S_6^{2-}} - \varepsilon_1 k_f \left(C_{1,S_6^{2-}} - \frac{C_{1,S_3^{*}}^2}{K_{S_3}} \right)$ $\frac{\partial \varepsilon_1 C_{1,S_3^{*}}}{\partial t} = -\frac{\partial N_{1,S_3^{*}}}{\partial x} + 2\varepsilon_1 k_f \left(C_{1,S_6^{2-}} - \frac{C_{1,S_3^{*}}^2}{K_{S_3}} \right)$ $N_{1,i} = -D_{1,i} \frac{\partial C_{1,i}}{\partial x} - z_i \frac{D_{1,i}}{RT} F C_{1,i} \frac{\partial \phi_{1,e}}{\partial x}$ $i_s = -\sigma \frac{\partial \phi_s}{\partial x}$ $i_{1,e} = F \sum_j z_j N_{1,j}$ $\frac{\partial \varepsilon_{1,k}}{\partial t} = V_k R'_k$ $\frac{\partial \varepsilon_{1,k}}{\partial t} = -\sum_k \tilde{V}_k R'_k$	$C_{1,i} \Big _{x=l_1} = C_{2,i} \Big _{x=l_1}$ $N_{1,i} \Big _{x=0} = 0$ $-\sigma \frac{\partial \phi_s}{\partial x} \Big _{x=0} = i_{app}$ $i_{1,e} \Big _{x=0} = 0$ $N_{1,i} \Big _{x=l_1} = N_{2,i} \Big _{x=l_1}$ $-\sigma \frac{\partial \phi_s}{\partial x} \Big _{x=l_1} = 0$
Separator (Region 2) $\frac{\partial \varepsilon_2 C_{2,Li}}{\partial t} = -\frac{\partial N_{2,Li}}{\partial x}$ $\frac{\partial \varepsilon_2 C_{2,S_6^{2-}}}{\partial t} = -\frac{\partial N_{2,S_6^{2-}}}{\partial x} - \varepsilon_2 k_f \left(C_{2,S_6^{2-}} - \frac{C_{2,S_3^{*}}^2}{K_{S_3}} \right)$ $\frac{\partial \varepsilon_2 C_{2,S_3^{*}}}{\partial t} = -\frac{\partial N_{2,S_3^{*}}}{\partial x} + 2\varepsilon_2 k_f \left(C_{2,S_6^{2-}} - \frac{C_{2,S_3^{*}}^2}{K_{S_3}} \right)$ $N_{2,i} = -D_{2,i} \frac{\partial C_{2,i}}{\partial x} - z_i \frac{D_{2,i}}{RT} F C_{2,i} \frac{\partial \phi_{2,e}}{\partial x}$ $i_{2,e} = F \sum_j z_j N_{2,j}$ $\frac{\partial \varepsilon_{2,k}}{\partial t} = V_k R'_k$ $\frac{\partial \varepsilon_{2,k}}{\partial t} = -\sum_k \tilde{V}_k R'_k$	$N_{2,Li} \Big _{x=l_1+l_2} = \frac{i_{app}}{F}$ $N_{2,i} \Big _{x=l_1+l_2} = 0$ $i_{2,e} \Big _{x=l_1} = i_{2,e} \Big _{x=l_1}$ $\phi_s \Big _{x=l_1+l_2} = 0$ $i_{2,e} \Big _{x=l_1+l_2} = F N_{2,Li}$
Other expressions $r_i = -a \sum_j \frac{s_{ij}}{n_j F}$ $\frac{\partial \phi_s}{\partial x} + \frac{\partial \phi_e}{\partial x} = 0$ $n_j = \phi_s - \phi_e - U_{j,ref}$ $R_i = \sum_k \gamma_{i,k} R'_k$ $i_j = i_{0,j,ref} \left[\left(\frac{C_{1,anodic}}{C_{1,ref}} \right)^{s_{a,j}} \exp \left(\frac{\alpha_{a,j} F}{RT} \eta_j \right) - \left(\frac{C_{1,cathodic}}{C_{1,ref}} \right)^{-s_{c,j}} \exp \left(-\frac{\alpha_{c,j} F}{RT} \eta_j \right) \right]$	$a = a_0 \left(\frac{\varepsilon}{\varepsilon_{initial}} \right)^{\frac{1}{2}}$ $\frac{\partial \phi_s}{\partial x} = a \sum_j i_j$ $U_{j,ref} = U_j^0 - \frac{RT}{n_j F} \sum_i s_{ij} \ln \left[\frac{C_i}{1000} \right]$ $R'_k = k_k \varepsilon_k \left(\prod_i C_i^{\gamma_{i,k}} - K_{sp,k} \right)$

[a] Please see the Supporting Information for the list of symbols.

Table 3. Properties of the electrochemical reactions.

Reaction [j]	$i_{0,j,ref}$ [A/m ²]	U_j^0 [V]	$s_{a,j}$	$s_{c,j}$	$\alpha_{a,j}$	$\alpha_{c,j}$
2	1.972	2.50	-1/2	1/2	1/2	1/2
3	0.019	2.49	-3/2	2	1/2	1/2
4	0.019	2.42	-1	3/2	1/2	1/2
5	1.97×10^{-4}	2.12	-1/2	1	1/2	1/2
6	1.97×10^{-7}	2.00	-1/2	1	1/2	1/2

Table 4. Parameters for the Ionic Species.

Species (i)	z_i	D_{i0} [m ² /s]	$C_{i,ref}$ [mol/m ³]
Li ⁺	+1	1×10^{-11}	1033
$S_{8(l)}$	0	1×10^{-10}	19.9
S_8^{2-}	-2	6×10^{-11}	0.16
S_6^{2-}	-2	6×10^{-11}	0.31
S_4^{2-}	-2	1×10^{-11}	0.020
S_2^{2-}	-2	1×10^{-11}	0.56×10^{-6}
S_3^{*}	-2	1×10^{-11}	0.78×10^{-9}
A ⁻	-1	7×10^{-10}	1032
S_3^{*-}	-1	1×10^{-11}	1×10^{-4}

original values from the Kumaresan et al. model. Here, base case simulation refers to the original chemical speciation given by Kumaresan et al., where no radical anion forms; this is achieved by setting the dissociation rate parameter to $k_f=0$ in Equations (3) and (4). Figure 2 shows that the new base case

Parameter	Cathode	Separator
a_0 [m^2/m^3]	143292	–
$\epsilon_{\text{initial}}$	0.6	0.6
$\epsilon_{S_{8(s)}, \text{initial}}$	0.24	1×10^{-12}
$\epsilon_{Li_2S_{(s)}, \text{initial}}$	1×10^{-7}	1×10^{-7}
σ	937	–
ξ	1.5	–
T [K]	293	293
b	2.5	2.5

Precipitate (k)	Rate constant (k_r)	Solubility product ($K_{sp, k}$)	Molar volume (V_k) [m^3/mol]
$S_{8(s)}$	1.0 s^{-1}	20 mol m^{-3}	1.239×10^{-4}
$Li_2S_{(s)}$	$27 \text{ m}^6 \text{ mol}^2 \text{ s}^{-1}$	$2.8 \times 10^{-5} \text{ mol}^3 \text{ m}^{-9}$	2.768×10^{-5}

parameters lead to a longer and higher initial voltage plateau at discharge capacities below 2 mAh/cm². In Figure 2a, the two modeled curves are compared at a low discharge rate of 0.2 C, and they have similar final discharge capacities greater than 8 mAh/cm² before reaching the end of discharge voltage cut-off. As the C rate is increased to 0.5 C (Figure 2b) and 1.0 C (Figure 2c), the total capacity of the battery represented by the new base case parameters declines, matching what is generally observed in the experimental literature for high energy density cells. In contrast, the Kumaresan et al. curves in Figure 2 are independent of rate, retaining more than 8 mAh/cm² of capacity for all discharge rates. In all subsequent analysis, we will use the new base case parameters as we explore the role radical anion chemistry on the discharge behavior of the cell. While the reversible dissociation chemistry represented by Equation (1) and embodied in species balance Equations (3) and (4) involves no charge transfer, the new radical anion represents a sink for partially reduced sulfur that can impact performance. The dissociation rate parameter k_f has units of inverse seconds, and dictates the timescales over which reversible Equation (1) comes to equilibrium, whereas the equilibrium dissociation constant, K_{S_3} , with units of mol/m³, determines the overall ratio of the two polysulfide species at equilibrium.

Figure 3 shows the effect of the equilibrium dissociation constant on the 1 C battery discharge curves when the reaction kinetics are fast. Here the kinetics are deemed fast because a 1 C discharge takes 3600 s, whereas the time for Equation (1) to achieve equilibrium scales as $\sim O(1/k_f)$, or milliseconds for a rate constant of $k_f = 1000 \text{ s}^{-1}$. For comparison, Figure 3a also includes the new base case curve from figure 2c (where $k_f = 0$). Figure 3b emphasizes the impact of dissociation equilibrium on the discharge curve voltages by showing potential differences between each of the curves with dissociation chemistry and the base case simulation in Figure 3a. With a value of $K_{S_3} < 1000 \text{ mol/m}^3$, the dissociation equilibrium strongly favors S_6^{2-} , diminishing the role of the radical anion product on the voltage curve. The resulting discharge curve is minimally perturbed when equilibrium favors the same speciation as the base case.

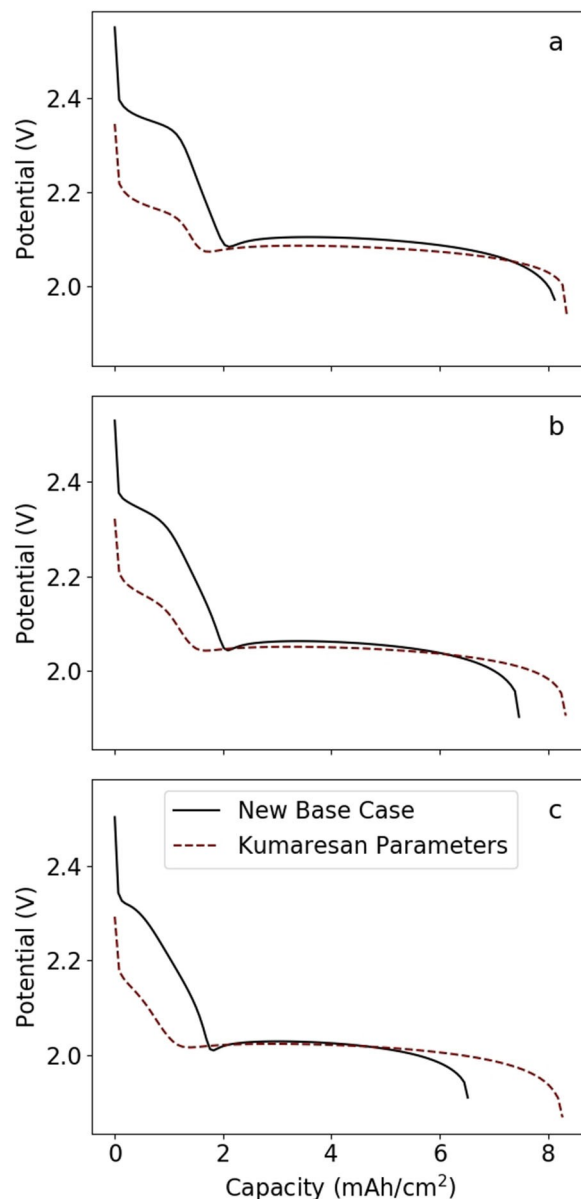


Figure 2. Comparison of the new base case parameters (—) developed here and the Kumaresan et al. parameters (---) for the discharge rates: a) 0.2C, b) 0.5C, and c) 1.0C. No new dissociation chemistry is considered here (i.e., $k_f = 0$ for the base case).

However, as K_{S_3} increases, reaction equilibrium increasingly favors the formation of radical anion, creating an increasingly concentrated pool of partially reduced sulfur species that is not directly involved in the reduction cascade on the cathode. Once there is a significant pool of radical anion, the reaction cascade is altered. Figure 3a shows that the voltage of the first plateau near 2.35 V is enhanced by more than 50 mV as the electrolyte favors partitioning to the radical anion rather than its dimer. This voltage support is followed by a rapid transition to the ~ 2 V second plateau. During the transition to the second voltage plateau, the voltage deviations away from the base case can be depressed by nearly 200 mV. In Figure 3b, the transition between enhancing cell voltage (up to discharge

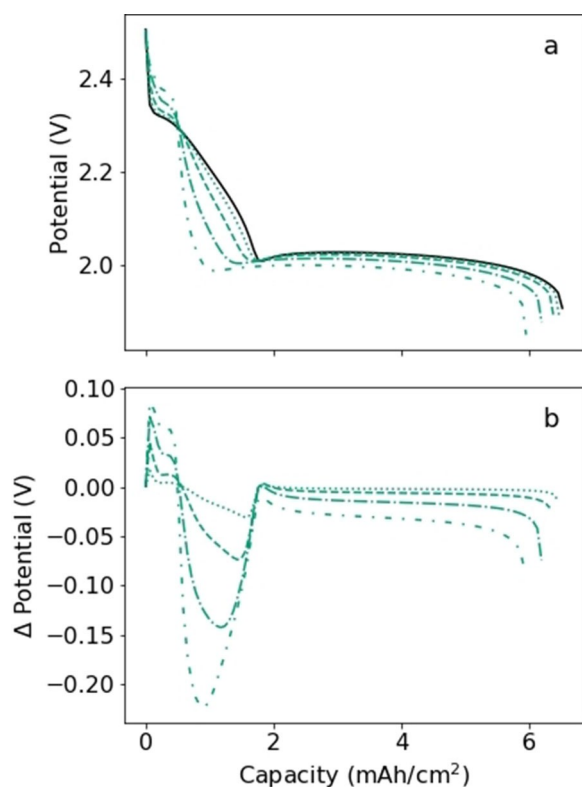


Figure 3. a) The 1C discharge curves for fast dissociation kinetics ($k_f = 1000 \text{ s}^{-1}$) and increasing equilibrium coefficients $K_{S_3} = 10^3 \text{ mol/m}^3$ (•••), 10^4 mol/m^3 (---), 10^5 mol/m^3 (—•—•—), and 10^6 mol/m^3 (-•-•-) are compared to the base case without any dissociation chemistry ($k_f = 0$, —). b) Potential difference between each fast dissociation discharge curve and the base case.

capacities of roughly 0.75 mAh/cm^2) and depressing cell voltage (all discharge capacities greater than 0.75 mAh/cm^2) is a marker of the average sulfur redox state of the battery compared to the redox state of the polysulfide species in Equation (1). Specifically, the per sulfur partial charge for both species in Equation (1) is -0.33 . As the battery discharges, the average partial charge progresses from elemental sulfur (0 per sulfur charge) to the final $\text{Li}_2\text{S}_{(s)}$ discharge product with per sulfur charge of -2 . The cell voltage is enhanced in the early stages of discharge when electrolyte speciation is dominated by less-reduced polysulfides than found in Equation (1), and depressed when discharge progresses to more reduced forms of polysulfides.

In terms of electrolyte engineering, a rising K_{S_3} value corresponds to an electrolyte that has increasingly better solvation and stabilization of the radical anion $\text{S}_3^{\bullet-}$ compared to its dimer anion the S_6^{2-} species. Gupta et al.^[17] identifies two solvents with the characteristic blue optical signature of the $\text{S}_3^{\bullet-}$ radical species, *N,N*-dimethylacetamide (DMA) and dimethyl sulfoxide (DMSO). The stable presence of $\text{S}_3^{\bullet-}$ radical implies a high K_{S_3} for these electrolytes. Alternately, S_6^{2-} was found to be favored in 1-methylimidazole (Melm) and a 1:1 by volume mixture of 1,2-dimethoxyethane (DME) and 1,3-dioxolane (DOL) electrolytes (*i.e.*, these electrolytes had low K_{S_3}). Likewise, model fits to cyclic voltammetry experiments in DME:DOL electrolyte

also produced K_{S_3} values that favored S_6^{2-} formation.^[40] Unfortunately, simple molecular descriptors of a solvent such as its donor number, appear inadequate for *a priori* prediction of which polysulfide species will be preferentially solvated.^[17]

While thermodynamic effects dominated in Figure 3, where the kinetics are fast, rather different behavior is seen in Figure 4 when we examine 0.5C discharge with slow dissociation kinetics of $k_f = 0.001 \text{ s}^{-1}$. Here, the time constant for the dissociation kinetics is of the order 1000 s, making it comparable to the cell discharge time of 7200 s. In this case, it takes a significant fraction of the discharge before any radical anion can build up via the forward dissociation chemistry of Equation (1). Thus, even when the equilibrium dissociation constant strongly favors the formation of radical anion (e.g., $K_{S_3} = 10^6 \text{ mol/m}^3$), there is no appreciable change to the discharge curve until roughly 1000 s have elapsed, or $1/7^{\text{th}}$ of the capacity has been discharged. Thus, unlike the situation in Figure 3, the early discharge voltage is not enhanced in Figure 4. However, Figure 4 does show appreciable depression of the voltage at longer discharge times (compared to the base case) for large values of K_{S_3} where radical anion is favored thermodynamically. This has a deleterious effect on the extractable energy from the cell. Likewise, the capacity can be appreciably decreased for the slow kinetic case when there is favorable partitioning toward radical anion, as seen in Figure 4,

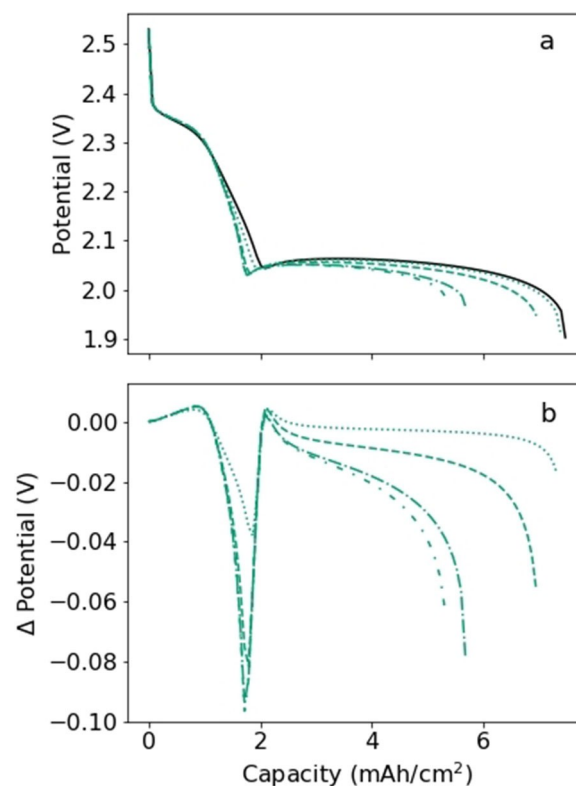


Figure 4. a) The 0.5C discharge curves for slow dissociation kinetics ($k_f = 0.001 \text{ s}^{-1}$) and increasing equilibrium coefficients $K_{S_3} = 10^3 \text{ mol/m}^3$ (•••), 10^4 mol/m^3 (---), 10^5 mol/m^3 (—•—•—), and 10^6 mol/m^3 (-•-•-) are compared to the base case without any dissociation chemistry ($k_f = 0$, —). b) Potential difference between each slow dissociation discharge curve and the base case.

owing to lower sulfur utilization when polysulfide inventory gets “stuck” in the slow converting radical anion. Unlike the fast kinetic case, where cell voltage was enhanced at low depth of discharge, slow kinetics at best have little impact and at worst depress voltages and decrease capacity.

Finally, we will consider the effect of a wide range of dissociation rate constants k_f in greater detail when the electrolyte favors partitioning toward the radical anion via a high value of $K_{S_3} = 100,000 \text{ mol/m}^3$. Figure 5a shows a series of 0.5 C discharge curves with varying k_f values. With the lowest value of $k_f = 10^{-5} \text{ s}^{-1}$, the voltage curve essentially follows the base case ($k_f = 0$) and there is no inventory of radical anion in the cell over the 7200 second discharge time. As the dissociation

kinetics increase, the voltage curve has a higher initial voltage plateau with a steeper slope and earlier transition to the second plateau, mirroring the behavior seen in Figure 3.

Figure 5b shows the total molar inventory of radical anion from Equation (1) that accumulates in the cell during the 0.5 C discharge (here the total radical anion inventory is given as moles per unit electrode area). Figure 5b shows this evolution of the radical anion $S_3^{\cdot-}$ inventory for the same parameters as in Figure 5a. For each of the simulations with a depressed discharge capacity (compared to the base case), there is significant radical anion $S_3^{\cdot-}$ inventory at the end of the discharge, representing trapped polysulfides that do not participate directly in charge transfer on the electrode. When an electrolyte design stabilizes the radical species, or forms any low reactivity polysulfides, capacity is lost in proportion to the inventory of that species at the end of discharge.

Figure 5c shows the spatial variation of the $S_3^{\cdot-}$ radical anion concentration across the separator (from 0 to $20 \mu\text{m}$ on the spatial axis) and the cathode regions ($20\text{--}120 \mu\text{m}$) when the kinetics are given as $k_f = 10^{-3} \text{ s}^{-1}$. The family of curves represent different depths of discharge (shown as % DOD in legend). From the profiles in Figure 5c, one sees continuous growth in the concentration of radical anion in the separator, whereas the cathode region has growth in radical anion until near the end of discharge, when it is seen to begin getting reconsumed by the back reaction in Equation (1). The general shape of the concentration profiles in Figure 5c are established very quickly compared to the discharge timescale; after only 5% discharge one sees the highest radical anion concentration is adjacent to the ideally-protected anode (at $0 \mu\text{m}$) and the concentration in the cathode is lower. This basic concentration profile persists at all subsequent discharge times. The separator concentration gradient is largely dictated by the no flux condition on the ideally-protected anode, where diffusion and migration must be equal and opposite. Only at discharge times that are short compared to the diffusion timescale across the separator (for $\text{DOD} < 1\%$, see S1a in Supporting Information) does the profile deviate significantly from this shape. The total inventory shown in Figure 5b is simply the integral of profiles such as these shown in Figure 5c. The spatial profiles of several other variables have been included in the Supporting Information, including the S_6^{2-} species profile, the volume fraction of $\text{Li}_2\text{S}_{(s)}$, and the cathode porosity.

It is interesting to note that the new speciation and assumptions embodied in Equation (1) lead to reversible capacity loss when a highly stable radical anion is generated. Figures 3–5 have illuminated the interplay of discharge timescale, reaction timescale, and equilibrium propensity for a species to dissociate through Equation (1). The experimental timescale explored here was set solely by the discharge C rate, which determined if the reaction timescale (inverse of k_f) was big or small. Thus, in Figure 5, we saw no appreciable change to the discharge curve (Figure 5a) and no accumulation of radical anion inventory (Figure 5b) over the 7200 s discharge time, when $k_f = 10^{-5} \text{ s}^{-1}$. Yet, ultraslow dissociation does not mean unimportant dissociation, especially when considering the aging of a partially discharged cell for days, weeks, or months.

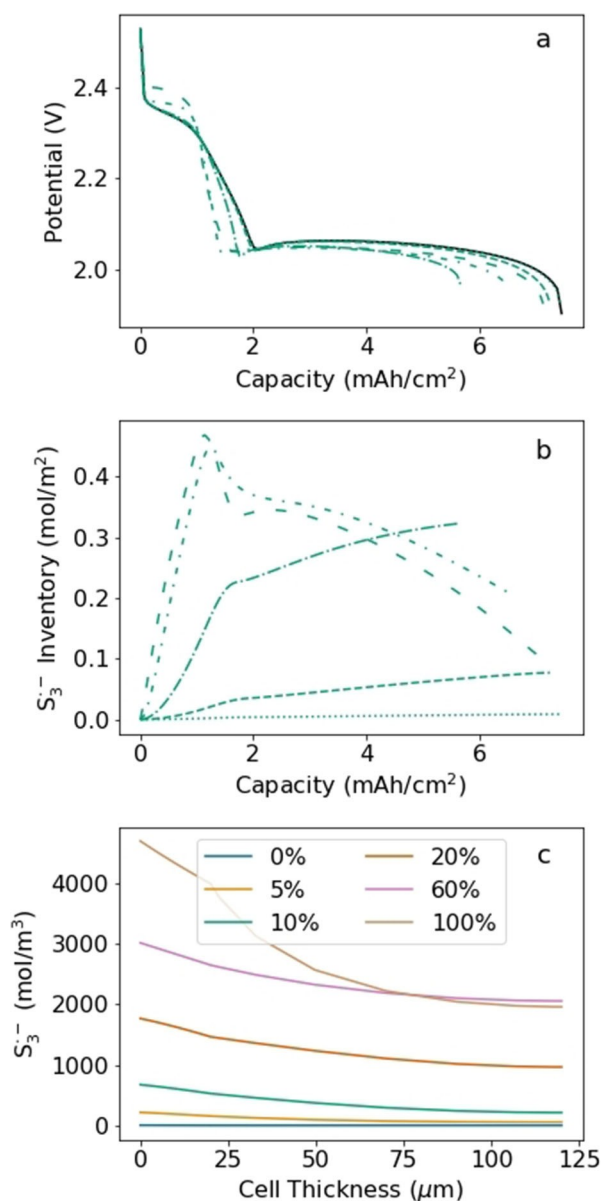


Figure 5. a) Effect of varying the dissociation rate constant k_f on the 0.5 C discharge curves when the equilibrium dissociation constant favors the radical anion ($K_{S_3} = 100,000 \text{ mol/m}^3$). b) Moles of radical anion per unit area of the full cell as a function dissociation rate constants. Curves represent $k_f = 0 \text{ s}^{-1}$ (—), 10^{-5} s^{-1} (•••), 10^{-4} s^{-1} (---), 10^{-3} s^{-1} (—•—•—),

In particular, consider a cell partially discharged to 1 mAh/cm² with $k_f = 10^{-5} \text{ s}^{-1}$. This cell will have negligible radical anion inventory when initially placed into storage (see Figure 5b), but over time, the inventory of S_6^{2-} will convert to S_3^{*} if K_{S_3} is large. When pulled from storage, the capacity and rate capability of the cell will have collapsed because so much sulfur inventory is in a stable, unreactive form. This collapse is reversible, but recovery of the active polysulfide is set by the dissociation kinetic timescale and would take a long trickle charge to restore the full capacity.

Conclusions

In this work, we have presented updated parameters that reflect the ongoing efforts to develop high-energy density lithium sulfur cells. The model suggests that incorporating insights from characterization of electrolyte speciation is required for subsequent LiS battery optimization. Experiments show that solvent choice can dramatically alter the equilibrium ratio of the two polysulfide species in Equation (1),^[17] meaning the choice of solvent either stabilizes the S_3^{*} radical (represented by higher K_{S_3} in our model) or the S_6^{2-} anion (lower K_{S_3} , here). Likewise, solvent-driven changes in the kinetics of Equation (1) can be associated with a lowering (high k_f) or raising (low k_f) the transition state activations energy. By including a reversible dissociation reaction to produce stable radical anion species seen experimentally, the electrochemical behavior of the cell was significantly changed. The equilibrium dissociation constant K_{S_3} and rate constant k_f influenced the timescale and propensity of the system to convert to a less active polysulfide form.

For dissociation timescales on the order of the voltage curve discharge times, the stabilization of radical anion led to decreased overall sulfur utilization since the species is not immediately available for reduction. All of the capacity loss was reversible, but we described storage scenarios and ultraslow conversion kinetics that might look like self-discharge attributed to irreversible reactions with the lithium metal anode. However, all our modeling assumed an ideally-protected anode that excluded any polysulfide reactions or corrosion of lithium, so no irreversible chemistry was possible here. Due to the complexity of this battery chemistry, there are numerous other dissociation and disproportionation reactions that might be considered for future work, as well as greater attention to the cathode hierarchical structure and imperfections in anode protection, if experimental studies highlight their critical role in the performance of the cell. Here, we highlighted a simple reaction involving a well-documented species that had heretofore been excluded in full-cell models, and laid out a clear pathway for closer collaboration between modeling and experimental work.

Finally, this work points to the need for additional attention to quantitative experimental measurements of the solvent-dependent dissociation and disproportionation reaction equilibrium and rate constants in concentrated electrolytes (near the polysulfide solubility limit), as found in low E/S ratio batteries. The growing body of experimental spectroscopy and electro-

analytical literature augurs well for battery-relevant quantitation of these parameters in the near future.

Computational Details

This work extends the standard model developed by Kumarasan et al.,^[20] with the polysulfide speciation and reduction cascade we call base case chemistry shown in Figure 1. At the lithium anode, there is a constant flux of lithium ions set by the C rate being evaluated. The anode is assumed to be ideally-protected with no side reactions considered and facile lithium cation transport.

Within the macrohomogeneous porous cathode, solid elemental sulfur dissolves to liquid sulfur as $S_{8(l)}$. The sulfur reduction cascade includes the five electrochemical reactions shown in the schematic. The only solid product considered is $Li_2S_{(s)}$ as there is still some debate about the presence of other solid products.^[30–31,51] The 1D physics-based model for lithium sulfur batteries incorporates thermodynamics, kinetics of electrochemical and precipitation reactions, transport described by the dilute solution theory, and morphology changes through the time dependence of the volume fractions and the porosities.

The subsequent set of differential algebraic equations (DAE), shown in Table 2, was solved in *Maple 2018* with the use of our robust DAE solver approach that combines initialization with DAE simulation as a single step. This uses the semi-implicit Runge Kutta built-in DAE solver called *dsolve* in implicit mode.^[52] The equation set was discretized using orthogonal collocation method with 7 node points for all simulations. Model self-convergence of less than 1% error was calculated using the average error of mid-point values in the cathode at $3/4$ discharge between simulations with $n=7$ and $n=9$. The initial conditions were found with the robust initialization strategy described in a previous study.^[53] The computational time for a typical discharge curve is 65 seconds on an AMD Ryzen 7 3700U processor with 16 GB RAM.

Supporting Information

The Supporting Information includes a table containing all the symbols used in the manuscript.

Acknowledgments

The authors would like to thank the Assistant Secretary for Energy Efficiency and Renewable Energy, Office of Vehicle Technologies of the U.S. Department of Energy through the Advanced Battery Materials Research (BMR) Program (Battery500 Consortium) and the Boeing-Sutter Endowment.

Conflict of Interest

The authors declare no conflict of interest.

Keywords: lithium-sulfur batteries · electrochemistry · modeling · energy storage · computational methods

- [1] T. Cleaver, P. Kovacic, M. Marinescu, T. Zhang, G. Offer, *J. Electrochem. Soc.* **2018**, *165*, A6029–A6033.
- [2] Z. Liu, A. Mistry, P. P. Mukherjee, *J. Electrochem. Energy Convers. Storage* **2018**, *15*, 10802.
- [3] Y. V. Mikhaylik, J. R. Akridge, *J. Electrochem. Soc.* **2004**, *151*, A1969.
- [4] Y. Diao, K. Xie, S. Xiong, X. Hong, *J. Power Sources* **2013**, *235*, 181–186.
- [5] S. Li, M. Jiang, Y. Xie, H. Xu, J. Jia, J. Li, *Adv. Mater.* **2018**, *30*, 1–29.
- [6] F. Y. Fan, W. C. Carter, Y.-M. Chiang, *Adv. Mater.* **2015**, *27*, 5203–5209.
- [7] A. Bhargav, J. He, A. Gupta, A. Manthiram, *Joule* **2020**, *4*, 285–291.
- [8] D. Lu, Q. Li, J. Liu, J. Zheng, Y. Wang, S. Ferrara, J. Xiao, J. G. Zhang, J. Liu, *ACS Appl. Mater. Interfaces* **2018**, *10*, 23094–23102.
- [9] R. Fang, S. Zhao, Z. Sun, D. W. Wang, H. M. Cheng, F. Li, *Adv. Mater.* **2017**, *29*, 1606823.
- [10] J. Brückner, S. Thieme, H. T. Grossmann, S. Dörfler, H. Althues, S. Kaskel, *J. Power Sources* **2014**, *268*, 82–87.
- [11] R. Xu, J. Lu, K. Amine, *Adv. Energy Mater.* **2015**, *5*, 1500408.
- [12] M. Barghamadi, A. S. Best, A. I. Bhatt, A. F. Hollenkamp, M. Musameh, R. J. Rees, T. Rütger, *Energy Environ. Sci.* **2014**, *7*, 3902–3920.
- [13] J. Cao, Q. Meisner, T. Glossmann, A. Hintennach, Y. Wang, P. Redfern, L. A. Curtiss, Z. Zhang, *ACS Appl. Mater. Interfaces* **2020**, *3*, 3198–3204.
- [14] J. Zheng, D. Lv, M. Gu, C. Wang, J.-G. Zhang, J. Liu, J. Xiao, *J. Electrochem. Soc.* **2013**, *160*, A2288–A2292.
- [15] H. L. Wu, L. A. Huff, A. A. Gewirth, *ACS Appl. Mater. Interfaces* **2015**, *7*, 1709–1719.
- [16] R. Bouchal, A. Boulaoued, P. Johansson, *Batteries & Supercaps* **2020**, *3*, 397–401; Supercaps **2020**, *3*, 397–401.
- [17] A. Gupta, A. Bhargav, A. Manthiram, *Adv. Energy Mater.* **2019**, *9*, 1803096.
- [18] É. Boros, M. J. Earle, M. A. Gilea, A. Metlen, A. V. Mudring, F. Rieger, A. J. Robertson, K. R. Seddon, A. A. Tomaszowska, L. Trusov, J. S. Vyle, *Chem. Commun.* **2010**, *46*, 716–718.
- [19] S. I. Tobishima, H. Yamamoto, M. Matsuda, *Electrochim. Acta* **1997**, *42*, 1019–1029.
- [20] K. Kumaresan, Y. Mikhaylik, R. E. White, *J. Electrochem. Soc.* **2008**, *155*, A576.
- [21] M. Ghaznavi, P. Chen, *J. Power Sources* **2014**, *257*, 394–401.
- [22] M. Ghaznavi, P. Chen, *J. Power Sources* **2014**, *257*, 402–411.
- [23] M. Ghaznavi, P. Chen, *Electrochim. Acta* **2014**, *137*, 575–585.
- [24] J. P. Neidhardt, D. N. Fronczek, T. Jahnke, T. Danner, B. Horstmann, W. G. Bessler, *J. Electrochem. Soc.* **2012**, *159*, A1528–A1542.
- [25] D. N. Fronczek, W. G. Bessler, *J. Power Sources* **2013**, *244*, 183–188.
- [26] A. F. Hofmann, D. N. Fronczek, W. G. Bessler, *J. Power Sources* **2014**, *259*, 300–310.
- [27] T. Danner, G. Zhu, A. F. Hofmann, A. Latz, *Electrochim. Acta* **2015**, *184*, 124–133.
- [28] T. Zhang, M. Marinescu, L. O'Neill, M. Wild, G. Offer, *Phys. Chem. Chem. Phys.* **2015**, *17*, 22581–22586.
- [29] D. Moy, A. Manivannan, S. R. Narayanan, *J. Electrochem. Soc.* **2015**, *162*, A1–A7.
- [30] M. Marinescu, T. Zhang, G. J. Offer, *Phys. Chem. Chem. Phys.* **2016**, *18*, 584–593.
- [31] T. Zhang, M. Marinescu, S. Walus, G. J. Offer, *Electrochim. Acta* **2016**, *219*, 502–508.
- [32] K. Yoo, M. K. Song, E. J. Cairns, P. Dutta, *Electrochim. Acta* **2016**, *213*, 174–185.
- [33] N. Kamyab, P. T. Coman, S. K. Madi Reddy, S. Santhanagopalan, R. E. White, *J. Electrochem. Soc.* **2020**, *167*, 130532.
- [34] Y. X. Ren, T. S. Zhao, M. Liu, P. Tan, Y. K. Zeng, *J. Power Sources* **2016**, *336*, 115–125.
- [35] A. N. Mistry, P. P. Mukherjee, *J. Phys. Chem. C* **2018**, *122*, 18329–18335.
- [36] M. Marinescu, L. O'Neill, T. Zhang, S. Walus, T. E. Wilson, G. J. Offer, *J. Electrochem. Soc.* **2018**, *165*, A6107–A6118.
- [37] J. Shim, T. J. Ko, K. Yoo, *J. Ind. Eng. Chem.* **2019**, *80*, 283–291.
- [38] C. D. Parke, A. Subramaniam, S. Kolluri, D. T. Schwartz, V. R. Subramanian, *J. Electrochem. Soc.* **2020**, *167*, 163503.
- [39] V. Thangavel, K. Xue, Y. Mammeri, M. Quiroga, A. Mastouri, C. Gu, P. Johansson, M. Morcrette, A. A. Franco, *J. Electrochem. Soc.* **2016**, *163*, A2817–A2829.
- [40] V. Thangavel, A. Mastouri, C. Guéry, M. Morcrette, A. A. Franco, *Batteries & Supercaps* **2020**, 152–162.
- [41] F. Gaillard, E. Levillain, M. C. Dhamelincourt, P. Dhamelincourt, J. P. Lelieur, *J. Raman Spectrosc.* **1997**, *28*, 511–517.
- [42] B. Kim, S. Park, *J. Electrochem. Soc.* **1993**, *140*, 115–122.
- [43] D.-H. Han, B.-S. Kim, S.-J. Choi, Y. Jung, J. Kwak, S.-M. Park, *J. Electrochem. Soc.* **2004**, *151*, E283–E290.
- [44] F. Gaillard, E. Levillain, J. P. Lelieur, *J. Electroanal. Chem.* **1997**, *432*, 129–138.
- [45] Z. Wang, Y. Tang, X. Fu, J. Wang, Z. Peng, L. Zhang, J. Huang, *ACS Appl. Mater. Interfaces* **2020**, *12*, 55971–55981.
- [46] Q. Zou, Z. Liang, G. Y. Du, C. Y. Liu, E. Y. Li, Y. C. Lu, *J. Am. Chem. Soc.* **2018**, *140*, 10740–10748.
- [47] C. Barchasz, F. Molton, C. Duboc, J. C. Leprêtre, S. Patoux, F. Alloin, *Anal. Chem.* **2012**, *84*, 3973–3980.
- [48] H. Shin, M. Baek, A. Gupta, K. Char, A. Manthiram, J. W. Choi, *Adv. Energy Mater.* **2020**, *10*, 1–21.
- [49] J. Xie, Y. W. Song, B. Q. Li, H. J. Peng, J. Q. Huang, Q. Zhang, *Angew. Chem. Int. Ed.* **2020**, *59*, 22150–22155.
- [50] S. Walus, C. Barchasz, R. Bouchet, J. C. Leprêtre, J. F. Colin, J. F. Martin, E. Elkaïm, C. Baehtz, F. Alloin, *Adv. Energy Mater.* **2015**, *5*, 1500165.
- [51] R. N. Methkar, V. Ramadesigan, J. C. Pirkle, V. R. Subramanian, *Comput. Chem. Eng.* **2011**, *35*, 2227–2234.
- [52] M. T. Lawder, V. Ramadesigan, B. Suthar, V. R. Subramanian, *Comput. Chem. Eng.* **2015**, *82*, 283–292.
- [53] V. R. Subramanian, V. Ramadesigan, P. W. C. Northrop, S. De, B. Suthar, M. T. Lawder, *Systems and Methods for Improving Battery Performance*, **2018**, US 10,037,395 B2.

Manuscript received: December 14, 2020

Revised manuscript received: February 18, 2021

Accepted manuscript online: February 26, 2021